Microstructure and Corrosion Resistance of Electrophoretic Deposited Carbonated Hydroxyapatite-Graphene Oxide Composite Coatings on AZ91 Magnesium Alloy

Zishan Chen, Wei Wang[*]*, Qimin Liang, Weiming Lin*

School of Materials Engineering, Shanghai University of Engineering Science, Shanghai, 201620, China
[*]E-mail: wangwei200173@sina.com

Carbonated hydroxyapatite-graphene oxide (GO) composite coatings were obtained on AZ91 magnesium alloy using electrophoretic deposition from isopropanol suspensions. The results showed that ultrasonic treatment exfoliated GO sheets and promoted CO_2 adsorption on the surface of GO sheets. Subsequently, B-type carbonated HA was generated during ultrasonication-assisted EPD. The experimental results manifested that microstructures and porosity, carbonated HA content and the formation of GO-Mg complexes in pores/cracks had a significant synergistic effect on improving corrosion resistance of AZ91 magnesium alloy. HA-GO-0.33 composite coating had shown superior performance of corrosion prevention in the 0.9 wt. % NaCl solution which provided some corrosion theoretical basis for the application of Mg alloy in the direction of human implantation.

Keywords: Magnesium alloy; Graphene oxide; Carbonated hydroxyapatite; Corrosion resistance; Electrophoretic

1. INTRODUCTION

Magnesium (Mg) alloys are advanced lightweight materials, which have been used widely in automobile, 3C products and aerospace industries [1-4]. In recent years, Mg alloys have attracted great attentions as a potential biodegradable material, such as bone implant and regeneration [5-7]. However, before Mg alloys used in biomedical applications, their corrosion resistance in the physiological environment must be improved.

In order to improve the corrosion resistance of Mg alloy, metallurgical methods have been developed to prevent it from being corroded based on the alloy itself, including homogenization [8], alloying [9,10] and doping rare metals [11]. However, these methods are not effective in inhibiting galvanic corrosion. In addition, many surface treatments have been applied to prepare protective

coatings on the Mg alloy substrates, preventing the contact between corrosion medium and Mg alloy. Previous studies have shown that Hydroxyapatite (HA, $Ca_{10}(PO_4)_6(OH)_2$) can effectively improve the corrosion resistance and biocompatibility of Mg alloy [12,13]. However, it is relatively difficult to directly deposit HA coatings on Mg alloy substrate owing to the lack of agglomerated sites for HA growth. In addition, HA coatings tend to result in the propagation of cracks due to relatively low mechanical strength and fracture toughness, thus increasing corrosion rate [14].

It has been well documented that carbonated hydroxyapatite (carbonated HA) demonstrates better biocompatibility and osteoconductive properties than HA due to its crystal structure similar to human bone tissue [15]. The presence of carbonate ions in the hydroxyapatite lattice has proved to be a good strategy to improve mechanical properties and increase solubility [16]. Carbonated HA can be directly transformed by high temperature solid-state transformation in CO_2 atmosphere [17] or by wet chemical precipitation [18-20].

It has been reported that GO possesses good biocompatibility [21]. Additionally, studies have shown that oxygen functional groups of GO can provide abundant agglomerated sites, thus promoting the agglomeration of HA [22-24]. Moreover, the surface functionality of GO has been used as a potential CO_2 adsorbent due to the possible interaction between the unsaturated sp^2 bonded carbon honeycomb lattice structure at the edge of GO basal plane with CO_2 through electrostatic force [25,26].

A variety of techniques have been used to prepare HA/GO composite coatings, including plasma spraying (PSP) [27], chemical vapor deposition (CVD) [28,29], solution spray coating [30], dip coating [31,32], vacuum filtration [33], spin coating [32], brushing [34] and electrophoretic deposition (EPD) [35-37], among which PSP and CVD are the most widely used. However, PSP not only results in HA decomposition at high temperature [38, 39], but also does not uniformly coat complex shaped substrates [40]. CVD deposits slowly and thus cannot be used to prepare thick coatings. The solution-based coating methods for preparing thick coatings have been explored [41]. Nevertheless, the prepared thick coatings have poor bond strength to the metal substrate [42]. EPD was developed HA-GO composite coatings owing to high cost efficiency, simplicity and excellent bond strength to the metal substrate [43-45], which can control the thickness and uniformity of coatings by deposition voltage and time.

In this work, HA-GO composite coatings were prepared in isopropanol solution using EPD. The weak hydrogen bond between isopropanol and GO during ultrasonication was broken after the introduction of CO_2, and CO_2 interacted with the unsaturated sp^2 bonded carbon honeycomb lattice structure at the edge of GO basal plane with the help of electrostatic force.

Although HA-GO composite coatings have been studied by several research groups [46,47], to the best of our knowledge, there have not been systematic research on the effects of CO_2 adsorption via the exfoliated GO sheets on the transformation of HA into carbonated HA. In particular, composite coatings consisting of HA and carbonated HA were similar to that of bone tissue. Moreover, the formation of carbonates using CO_2 in the air as renewable carbonaceous materials is an attractive area of research.

In this paper, HA-GO composite coatings were prepared on Mg alloys using ultrasonication-assisted electrophoretic deposited method. The application of magnesium alloys in biodegradable materials and engineering has been expanded. Furthermore, the morphology and electro-chemical

corrosion tests of HA-GO composite coatings after 48 h of exposure in the 0.9 wt. % NaCl solution. In addition, the effects of the mass ratios of HA to GO and CO_2 adsorption via the exfoliated GO sheets on the morphology and corrosion characteristics of HA-GO composite coatings were systematically investigated.

2. EXPERIMENTAL

2.1. Sample preparations

In this work, AZ91 magnesium alloy (9 wt.% Al, 1 wt.% Zn, 0.17 wt.% Mn, 0.01 wt.% Fe and balanced Mg) in rectangular shape with a size of 20 mm × 20 mm × 3 mm was used as the substrate. Mg alloy substrates were firstly polished with SiC sandpapers up to 2000 grits before the coatings ultrasonication-assisted electrophoretic deposited on Mg alloy substrate. The substrate was mechanically ground with SiC sandpapers from 180 to 2,000 grits, degreased with alkaline solution (10 g/L $Na_3PO_4·12H_2O$ and 40 g/L NaOH) and then etched in 50 mL/L HNO_3 (70%) solution for about 30 s. Finally, washing in anhydrous ethanol and deionized water and dried at the ambient temperature.

A water-soluble calcium phosphate HA powder (Sinopharm Group,shanghai, China) was used to prepare the HA micro particles. The qualitative properties of the HA powder were analyzed by X-ray diffraction (XRD) to confirm that the prepared HA powder was similar to natural HA.

2.2. Graphene oxide synthesis

GO was manufactured using the modified Hummers method [48]. Firstly, flask equipped with a magnetic stirrer was filled with 57.5 mL of H_2SO_4. Then, the flask was placed into an ice bath while keeping the temperature under 10 °C. Subsequently, nano-graphite powder (2.5 g) was added slowly into the flask. Afterward, $KMnO_4$ (1.5 g) was added slowly into the above mixture under vigorous stirring in an ice bath. Then, the suspension temperature was raised to 35 °C, and the suspension was stirred for about 2 h until the mixture changed to thick green paste. The flask was then placed in an ice bath to cool the mixture, subsequently, 117.5 mL of deionized water was added slowly to the mixture, then the mixture was heated to 85 °C and stirred for 1 h. Afterward, 30 mL H_2O_2 (30 wt. %) was added slowly to assure that the $KMnO_4$ was reduced. The resulted suspension was then subjected to centrifuge at 10000 rpm to remove any aggregates. Finally, the synthesized GO was freeze dried in vacuum after washing with deionized water.

2.3. Preparation of HA-GO composite coatings

HA and GO suspension was prepared by magnetic stirring of mixture of GO in 50 mL of isopropanol solution. The suspension contained HA and GO particles or sheets with concentration of 1 mg/mL. The ultimate concentrations of GO in the suspension were 0.17, 0.33, 0.50, and 0.67 mg/mL,

respectively. Before EPD, the suspension was vigorously stirred for 10 min and sonicated for 1 h. The as-prepared HA-GO composite coatings were denoted as HA-GO-0.17, HA-GO-0.33, HA-GO-0.50, and HA-GO-0.67, respectively. For comparison, pure HA coating was prepared.
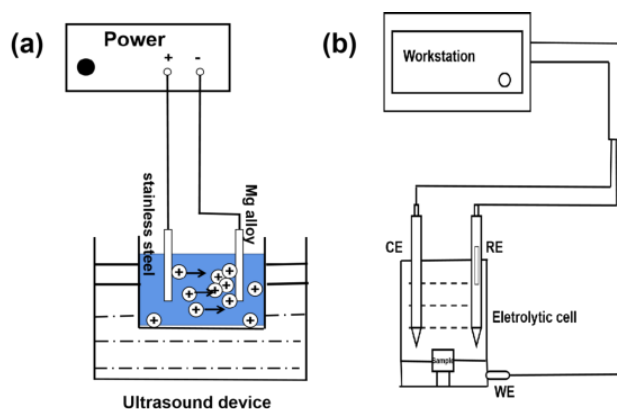

Figure 1. (a) Electrophoretic deposition (cEPD); (b) Electrochemical behavior.

EPD was performed by applying electric field between a stainless-steel plate (as anode) and a Mg alloy (AZ91) substrate (as cathode). The distance between the two electrodes was 2 cm. The deposition was carried out at a constant voltage of 120 V and duration of 3 min. After that, the samples were dried at room temperature for 2 h. The schematic diagram of the EPD process and the electrochemical behavior are shown in Fig. 1(a).

2.4. Characterization

The phase composition and surface morphological characterizations of AZ91 Mg alloy and coated specimens were determined with X-ray diffraction (XRD) and scanning electron microscope (SEM). The structural and chemical composition of AZ91 Mg alloy and coated specimens were analyzed with Fourier transform infrared (FT-IR) spectroscopy in the region of 4000–400 cm^{-1}.

The corrosion resistant properties of AZ91 Mg alloy and coated specimens were evaluated by using CHI650C electrochemical workstation in the 0.9 wt. % NaCl solution, as shown in Fig. 1(b). A classical three-electrode system consisting of a platinum plate served as counter electrode, electrode, a saturated calomel electrode (SCE) reference electrode was reference electrode, and AZ91 Mg alloy and coated specimens was used as working electrode with the exposed area of 1 cm^2. A platinum sheet was used as the auxiliary electrode counter electrode, and a saturated calomel electrode reference electrode was used as the reference electrode. Prior to start electrochemical tests, the working electrode was immersed in the 0.9 wt. % NaCl solution to assure the open circuit potential (OCP) to be stable. The polarization tests were conducted over the frequency from −0.7 V vs. OCP to +0.5 V vs. OCP at a scanning rate of 1 mV/s. EIS measurements were scanned from 0.01 Hz to 100 kHz using a signal with an amplitude of 1 mV. The experimental impedance plots were fitted by equivalent circuits using the Zview software. Each electrochemical measurement was repeated three times to ensure reproducibility.

3. RESULTS AND DISCUSSION

3.1. Phase composition analysis

Fig. 2 displays the XRD patterns of GO and HA nanopowders. The XRD pattern of GO nanopowders is presented in Fig. 2(a). As can be seen from the figure, the characteristic peak of $(001)_{GO}$ plane was observed at $2\theta = 11.3°$, corresponding to an interlayer spacing of 0.788 nm, which was caused by the presence of oxygen-containing functional groups.
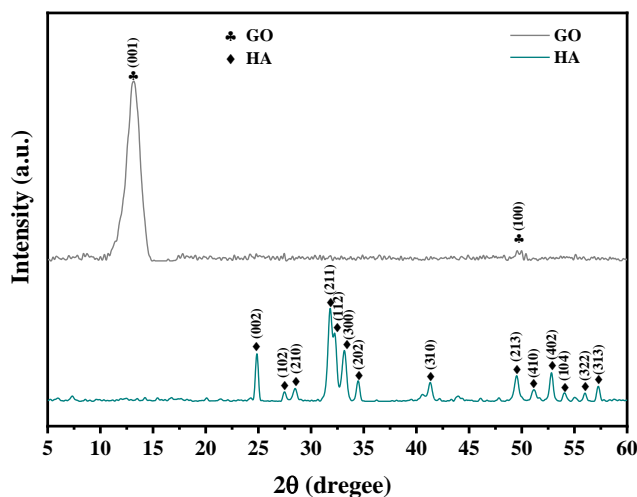

Figure 2. XRD patterns of the GO and HA nanopowders.

The weak peak at $2\theta = 42.3°$ was associated with graphitic powders in the GO nanopowders, indicating that there were still a few graphite powders in the GO nanopowders [49, 50]. The XRD pattern of HA powders is presented in Fig. 2(b), which shows that the HA nanopowders was a single-phase structure. And the diffraction peaks at 2θ of 25.8°, 31.7°, 32.1°, and 32.8° were respectively assigned to the $(002)_{HA}$, $(211)_{HA}$, $(112)_{HA}$ and $(300)_{HA}$ planes, which could be related to pure HA (PDF# 09-0432). According to the Scherrer equation, the grain size of the HA nanopowders was estimated to be about 12.37 nm.

Fig. 3 presents the XRD patterns of HA-GO composite coatings with different contents of GO. The main characteristic peak of $(211)_{HA}$ plane was observed at $2\theta = 31.7°$, without any precipitated phases. The addition of GO to the HA coating promoted the formation of HA-GO composite because epoxy- and carboxyl-functional groups of GO were bonded with Ca^{2+} ions of HA powders through coordinative covalent bonding or electrostatic attraction [50,51].
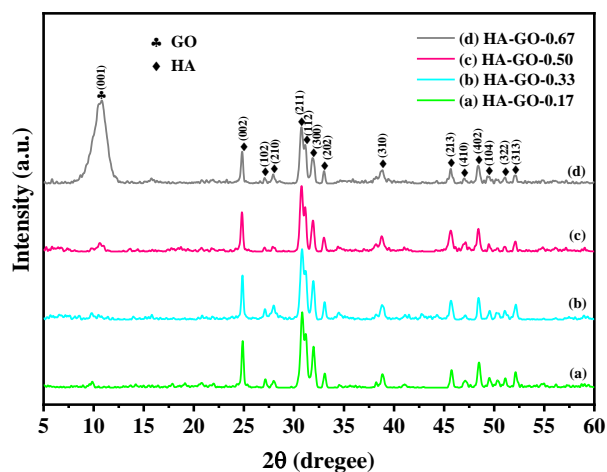
Figure 3. XRD patterns of the HA-GO composite coatings with the different GO content: (a) HA-GO-0.17 (b) HA-GO-0.33 (c) HA-GO-0.50 (d) HA-GO-0.67.

No obvious GO characteristic peaks were found between the XRD pattern of HA-GO-0.17, HA-GO-0.33 and HA-GO-0.50 composite coatings, as shown in Figs. 3(a), (b) and (c), which might be due to the less crystallographic order of GO nanopowders and irregular arrays of atoms in three dimensions because of sonicating during EPD or the masking of GO peaks by HA due to a lower content of GO than that of HA.

Despite there was no obvious difference between the pure HA and HA in the HA-GO composite coatings, there was a slight change in their unit cell parameters. The cell parameters were calculated by refining the XRD data using a standard least squares method. The corresponding lattice cell constants are listed in Table 1. According to the table, the c-axis remained unchanged, but the a-axis increased from 9.3684 Å to 9.4180 Å (Table 1).

Table 1. Lattice constants of HA and HA-GO

Samples	Lattice constants (Å)			Unit cell volume (Å^3)
	$a_0 = b_0$	c_0	c_0/a_0	
HA	9.3684	6.8841	0.735	523.25
HA-GO	9.4180	6.8840	0.731	528.80
Biological HA[57]	9.4190	6.8890	0.731	529.32

Compared with pure HA, the aspect ratio of HA c-axis/a-axis of HA-GO composite coatings slightly decreased. CO_3^{2-} ions have been reported to promote a-axis growth because of the interaction between CO_3^{2-} and calcium-rich a-plane [20]. It should be noted that the crystallographic behaviors of HA-GO composite coatings were similar to that of biological HA, indicating that the ultrasonication-assisted electrophoretic deposited technique is applicable to the fabrication of carbonated HA. Ultrasonic treatment exfoliated GO sheets and promoted CO_2 adsorption on the surface of GO sheets,

thereby improving the interaction between CO_3^{2-} and HA and inducing the formation of carbonated HA in HA-GO composite coatings in isopropanol solution during ultrasonication-assisted EPD.

The XRD patterns of HA-GO composite coatings were compared, as shown in Fig. 3. It can be seen from the figure that the diffraction peak corresponding to (001) plane of GO gradually shifted from a higher angle to a lower one with the increase in the content of GO additive. It is well known that the unsaturated sp^2 bonded carbon at the edge of GO basal plane interact with CO_2 with the help of electrostatic force [25,26], implying that the intercalation of CO_2 or CO_3^{2-} onto the GO coating promotes the exfoliation of GO sheets via bridging functional groups on the GO sheets. Compared with pure GO, the diffraction angles of the (001) plane in GO shifted from 11.3° to 10.81° for HA-GO-0.67, 10.59° for HA-GO-0.50, 9.77° for HA-GO-0.33 and 9.88° for HA-GO-0.17 coated samples. HA-GO-0.33 composite coating shifted to a much lower angle ($2\theta = 9.77°$) than other coated samples, suggesting the higher carbonate content in HA-GO-0.33 composite coating than that of other coated samples. According to the above results, the capacity of GO to capture CO_2 increased as follows: HA-GO-0.33 > HA-GO-0.17 > HA-GO-0.50 > HA-GO-0.67.

3.2. FTIR spectroscopy analysis of composite coatings

The FTIR spectrum of GO powder is displayed in Fig. 4. The peak of the synthesized GO at 3376 cm^{-1} was related to the O-H stretching vibration caused by the presence of hydroxyl groups (-OH) on the GO surface and interlayer water molecules. The characteristic peaks at 1700 cm^{-1} were associated with carboxyl groups (-COOH) on the edge of GO basal planes. The spectrum of GO in Fig. 4 shows the presence of oxygen-containing groups at 1030 cm^{-1} and 1226 cm^{-1}, which were respectively associated with the C-O and C-O-C stretching vibration. The oxygen-containing groups were formed due to the oxidation of graphite into GO sheets. Furthermore, the characteristic peaks at 1,606 cm^{-1} were related to un-oxidized part of the sp^2 carbon skeleton or adsorbed -OH in GO [52-54].

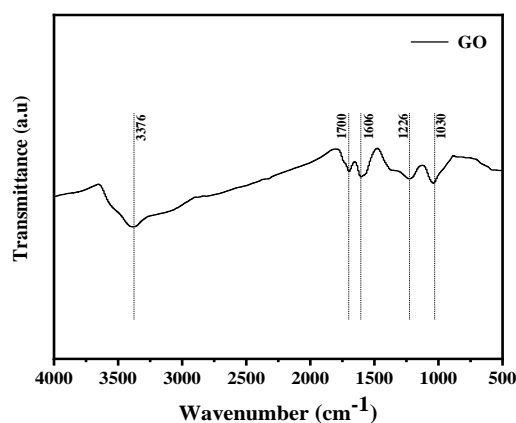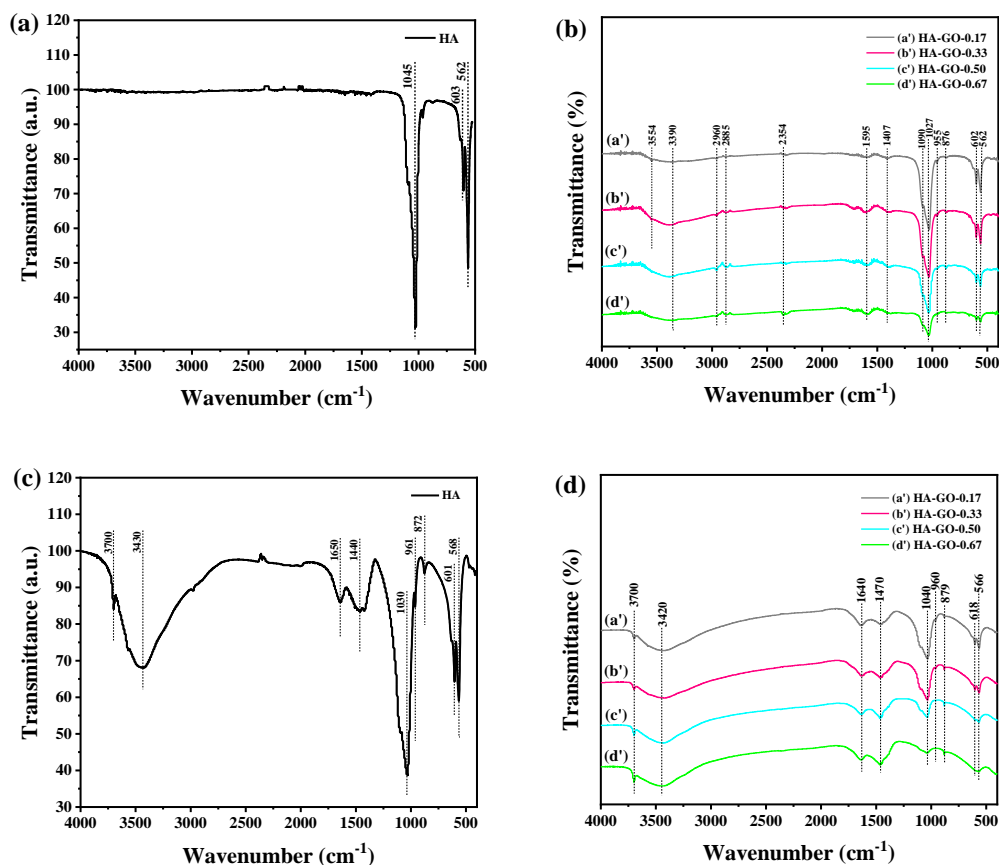**Figure 4.** FT-IR spectra of the GO powders.

Figure 5. FT-IR spectra of the (a) HA coating ;(b) HA-GO composite coatings ; (c) HA coating and (d) HA-GO composite coatings, after 48 hours of immersion in 0.9 wt. % NaCl solution.

Fig. 5 is the FTIR spectra of HA and HA-GO composite coatings before and after being immersed in the 0.9 wt. % NaCl solution with different contents of GO (the total weight of HA and GO was 50 mg) in 50 ml electrophoretic solution. The FTIR spectra of HA and HA-GO composite coatings before being immersed in the NaCl solution are shown in Figs. 5(a) and (b), respectively. Fig. 5(a) shows the bands for hydroxyapatite. The band at around 1045 cm^{-1} was related to υ_3 vibration of the PO_4^{3-} ions in pure HA coating, whereas, the $\upsilon4$ bending vibration of PO_4^{3-} groups appeared as the peaks at 562 and 603 cm^{-1}. The peak at 876 cm^{-1} was attributed to phosphate groups P-(OH) [55].

Meanwhile, the spectra of the HA-GO composite coatings before being immersed in the NaCl solution in Fig. 5(b) confirmed the presence of GO sheets by the emergence of some new absorption peaks of -CH_2 groups stretching vibration at 2960 and 2885 cm^{-1} [56]. The stretching band of the HA peaks showed a slight red-shifted from 1045 to 1027 cm^{-1}, indicating the hydrogen bonding between HA and GO sheets [56]. The peaks at 1090, 1027 and 955 cm^{-1} in the range of 1190 − 900 cm^{-1} were associated with the stretching modes of P-O bonds and those at 602, and 562 cm^{-1} were assigned to the bending modes O-P-O bonds. Compared with GO and HA coatings, FTIR spectra of the HA-GO composite coatings after EPD showed a wide absorption peak at 3390 cm^{-1} assigned to -OH stretching vibration. It can be observed that the -OH peak on HA-GO composite coatings was more intense than that on GO and HA, indicating newly formed carbonated HA on the surface of HA-GO composite

coatings, which is in good agreement with previous reports [57,58]. The additional absorption band at 2354 cm^{-1} peaks was related to the asymmetric stretching of CO_2 [59]. The characteristic absorption peaks at 1407 and 876 cm^{-1} corresponded to CO_3^{2-} group, indicating that HA-GO composite coatings prepared using EPD were mainly B-type carbonated HA, where PO_4^{3-} were substituted by CO_3^{2-} group [20,60], which was consistent with the XRD results (Figs. 2 and 3). B-type carbonated HA was verified as a natural mineral in bone tissue. The appearance of CO_3^{2-} group confirmed the partial decomposition of HA during EPD. Moreover, there were no peaks at 880 and 1544 cm^{-1} for A-type carbonate HA. It has been reported that A-type carbonated HA is generated at high temperatures in the presence of CO_2 when OH- ions are replaced by carbonate ions [61,62]. It should be noted that carbonate ions were not present in the electrolyte during EPD, but carbonated HA was formed from dissolved CO_2 in the air.

Moreover, as shown in Fig. 5(b), the absorption peaks of PO_4^{3-} at 1027 cm^{-1} were weakened, while the -OH peak on HA-GO composite coatings was more intense than that on GO and HA, indicating newly formed carbonated HA on the surface of HA-GO composite coatings, which is in good agreement with the previous reports [63,64]. It can also be clearly observed from Fig. 5(b) that when GO content was increased to 0.33 mg/mL, the intensity of the -OH peak at 3390 cm^{-1} of coated samples before immersion increased with the increase of GO content. When GO content was further increased to 0.67 mg/mL, the intensity of the -OH peak was gradually weakened, indicating that the substitution of carbonate ions into the HA lattice slightly decreased. It is in good agreement with the XRD result (Fig. 3). The results signify that the HA-GO-0.33 composite coating had a superior CO_2 adsorption capacity to other composite coatings, which was attributed to the easy CO_3^{2-} adsorption of exfoliated GO in HA-GO-0.33 composite coating [65].

As can be seen from the FTIR spectra of HA-GO-0.17 and HA-GO-0.33 composite coatings in Figs. 5(b), a'-d', the weak peak at 3554 cm^{-1} was assigned to -OH stretching vibration of HA coating [66,67]. The transmittance percentage of -OH stretching vibration decreased with the increase of GO content, implying that the formation of HA-GO composite. The above results are consistent with the XRD results. Comparing Fig. 4 with Fig. 5(b), it can be observed that the -COOH in GO disappeared and the asymmetrical stretching modes of carboxyl group (υ_{COO-}) appeared for HA-GO composite coatings, which were associated with the bond between carboxylate head and metal atom [25,68].

The FTIR spectra of HA and HA-GO composite coatings after immersion for 48 h in the 0.9 wt. % NaCl solution are shown in Figs. 5(c) and (d), respectively. In terms of HA coating, as shown in Fig. 5(c), the peak at 3700 cm^{-1} was attributed to the -OH stretching vibration of $Mg(OH)_2$, indicating the progress of substrate corrosion during ultrasonication-assisted electrophoretic deposited on Mg alloy [69]. It was reported that main corrosion product formed on the surface of Mg alloy in the NaCl solution was inner $Mg(OH)_2$ layer due to the Cl$^-$ and galvanic reaction [70]. Furthermore, the difference in the microstructures, urface porosity, content of B-type HA and the formation of and GO-Mg composite in the HA-GO composite coatings resulted in the difference in the amount of formed $Mg(OH)_2$ corrosion products in the order of HA-GO-0.67>HA-GO-0.17>HA-GO-0.50>HA-GO-0.33.

The absorption bands at 3430 cm^{-1} and 1650 cm^{-1} were assigned to the H-O-H symmetric stretching and bending vibration of water molecules due to the presence of absorbed water and interlayer water [71-73]. Additionally, the CO_3^{2-} peaks at 872 cm^{-1} and 1440 cm^{-1} was caused by PO_4^{3-}

substitution. However, the presence of CO_3^{2-} bands at 872 cm^{-1} and the disappearing of the -OH bands at 3554 cm^{-1} (Fig. 5(b)) were ascribed to AB-type substitution.

Fig. 5(d) shows the FTIR spectra of HA-GO composite coatings after immersion for 48 h in the 0.9 wt. % NaCl solution. The intensity of the -OH peaks at 3420 cm^{-1} was seen to be higher for HA-GO composite coatings after immersion, indicating newly formed carbonated HA on the surface of HA-GO composite coatings. The presence of the peak at 1470 cm^{-1} attributed to the vibrational bands of CO_3^{2-} groups of B-type carbonated HA further verified the above conclusion [58]. In contrast, only a negligible AB-type substitution was detected in HA coating, suggesting the dominant presence of B-type substitution in HA-GO composite coatings. The above results can infer that higher B-type substitution in HA-GO composite coatings might be attributed to the existence of enhanced CO_2 adsorption related to the exfoliated GO sheets, which agrees well with previous reports [63,64].

The HA-GO composite coatings before and after immersion in the 0.9 wt.% NaCl solution were compared, and the FTIR spectra of HA-GO composite coatings showed a shift in the position of the band associated with υ_{COO^-} towards higher wave numbers from 1595 to 1640 cm^{-1}, indicating that after the chelation of Mg/Ca ions with the carboxyl group in the GO sheets, metal atoms were further chemically bonded with the GO sheet to form more GO-Mg/Ca complexes [74,75].

3.3. Morphological features of the composite coatings

Fig. 6 shows surface morphological characterization of pure GO and HA-GO composite coatings with different GO contents. The morphology at the base and edge of GO is presented in Figs. 6(a) and (b). The results indicated that a large number of overlaps and folds appeared in the GO sheets after electrophoretic deposition, which could be related to the Van de Waals force and π-π interaction among the GO sheets, indicating the formation of GO coating after electrophoretic deposition.

The effect of GO content on the surface morphology of HA-GO composite coatings is presented in Figs. 6(c-j). In terms of HA-GO composite coating with the GO content of 0.17 mg/mL, GO sheets could not be differentiated easily from surface morphological characteristics of HA-GO-0.17 composite coating, as shown in Figs. 6(c) and (d), as these sheets were possibly covered with HA particles. Furthermore, as can be clearly seen from Figs. 6(c) and (d), microstructure of HA-GO composite coating with the GO content of 0.17 mg/mL was non-uniform and large particles were observed in some areas marked by arrows. HA particles were partially agglomerated, which were spherical in size of 10 μm.

However, with the increase of GO content, the size of HA particles decreased due to the presence of GO, making the surface of composite coating more compact and intact. As clearly shown in Figs. 6(e) and (f), when GO content was increased from 0.17 to 0.33 mg/mL, spherical HA particles were supported by GO layers, making particle size much smaller and composite coating more compact. The HA particles with the GO content of 0.33 mg/mL was around 5 μm in diameter, some of which were slightly agglomerated. The particle size of HA further decreased to less than 500 nm with the

increase of GO/HA ratio, as shown in Fig. 6(g-j). Meanwhile, the aggregation of HA was largely constrained with the increase of GO content.
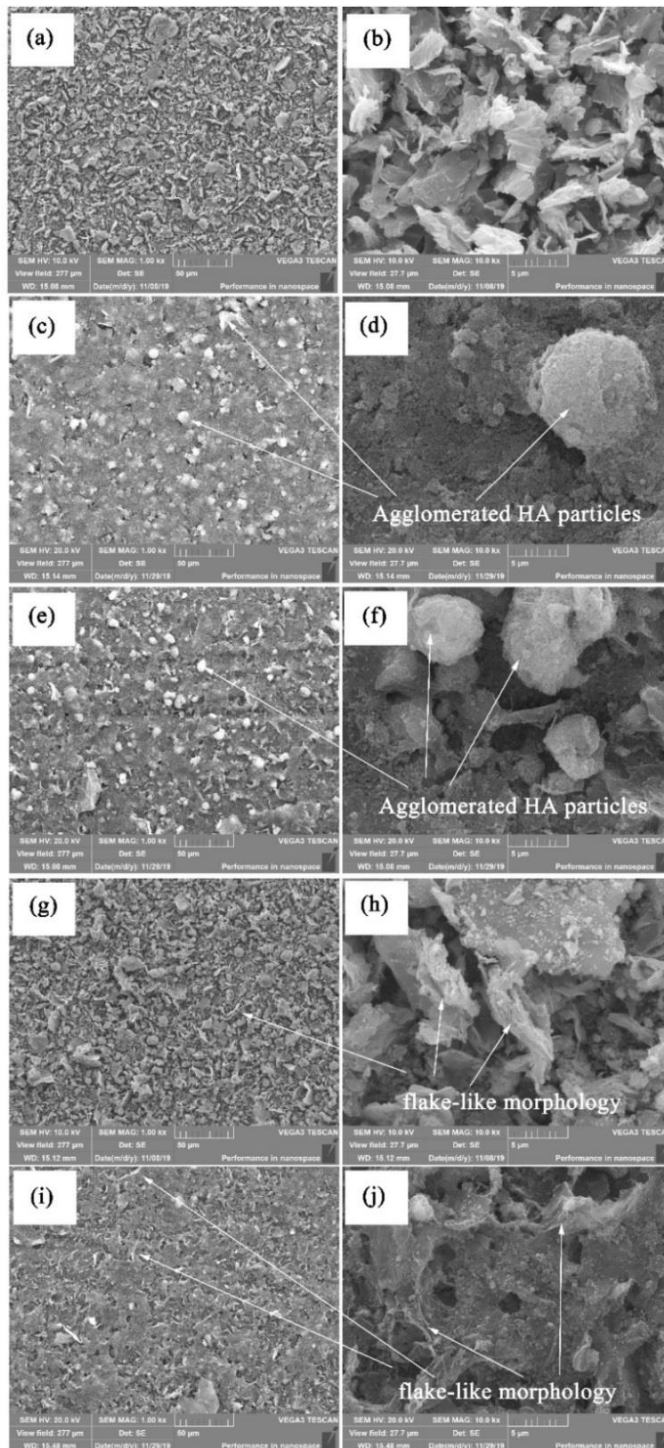

Figure 6. SEM images of the surface morphology of pure GO coating and HA-GO composite coatings with the different GO content: (a) (b) pure GO (a: x1000, b: x10000), (c) (d) HA-GO-0.17 (c: x1000, d: x10000), (e) (f) HA-GO-0.33 (e: x1000, f: x10000), (g) (h) HA-GO-0.50 (g: x1000, h: x10000), (i) (j) HA-GO-0.67 (i: x1000, h: x10000).

The decline in the size of the HA particles was attributed to the fact that GO sheets served as the agglomeration center for HA particles, leading to the formation of a refined and comparatively uniform composite coating. Generally speaking, the reduction of water induced the formation of -OH radicals during electrophoretic deposition, which resulted in the rising pH in the vicinity of the cathodically polarized Mg alloy substrate and the deprotonation of carboxyl and hydroxyl on the GO sheets. Correspondingly, GO sheets became more negatively charged. Hydroxyl and carboxyl promoted the electrostatic interaction of Ca^{2+} ions with GO sheets. Moreover, HA agglomerated and grew on the GO sheets through electrovalent bonds between PO_4^{3-} ions and Ca^{2+} ions [76,77]. In the process of electrophoretic deposition, GO sheets provided a large number of agglomerated sites of the HA particles, thus making HA particles smaller.

Obviously, with the decrease of particle size of HA, the pores/cracks of the composite coating also decreased. According to Fig. 6, the sizes of the micro-pores in the HA-GO composite coatings were significantly reduced when the GO content was increased from 0.17 to 0.67 mg/mL. Meanwhile, the pores gradually become smaller, as shown in Figs. 6(c-j). Furthermore, the addition of GO functionalized HA coating into an enhanced network, making HA-GO composite coating denser than HA coating. It was also found that the basal plane and edges of GO sheets for the composite coatings were very different from those of pure GO coating. As shown in Figs. 6(h) and (j), the adsorption of the HA on the GO sheets transformed the smooth morphology of pure GO sheets to rough one, including flake-like morphology. Figs. 6(g-j) show the flake-like morphology related to HA adsorbed on the surface of GO sheets. In addition, there were no obvious wrinkles on the GO sheets for the composite coatings. This uneven surface was in contrast to the clean and smooth surface of pure GO, indicating that the adsorption of HA significantly affected the surface morphology of GO sheets and the corrosion resistance of HA-GO composite coatings.

3.4. Electrochemical corrosion behaviors of composite coatings

The corrosion behaviors of AZ91 Mg alloy and coated Mg alloys were determined using Potentiodymanic polarization studies after immersion in the 0.9 wt. % NaCl solution for 48 h. Electrochemical parameters were derived from the polarization curves, including corrosion current density (i_{corr}), corrosion potential (E_{corr}), inhibition efficiency (IE %), breakdown potential (E_{bd}), anodic (β_a) and cathodic Tafel slopes (β_c). Generally speaking, E_{corr} indicates the tendency of the corrosion, and i_{corr} reflects corrosion rate. The higher values of E_{corr} and the lower values of i_{corr}, the better the anti-corrosion performance. E_{bd} indicates the capability of coated alloys to resist local corrosion [78]. The higher values of E_{bd}, the more stable the coating. The Stern-Geary equation Eq. (1) was used to calculate the polarization resistance (R_p) [79]. The larger values of R_p, the smaller the corrosion rate of the coatings. The value of IE% was calculated by Eq. (2) [80], i_{corr} and i^0_{corr} are the corrosion density of coated Mg alloy and AZ91 Mg alloy, respectively.

$$R_p = \frac{\beta_a \times \beta_c}{2.303 \times (|\beta_a| + \beta_c) \times i_{corr}} \qquad\qquad (1)$$

$$IE\% = \frac{i^0_{corr} - i_{corr}}{i^0_{corr}} \times 100 \qquad (2)$$

Fig. 7 shows the Potentiodynamic polarization curves of AZ91 Mg alloy, HA coating, and HA-GO composite coatings with different GO contents in the 0.9 wt. % NaCl solution. The corresponding electrochemical parameters are listed in Table 2.
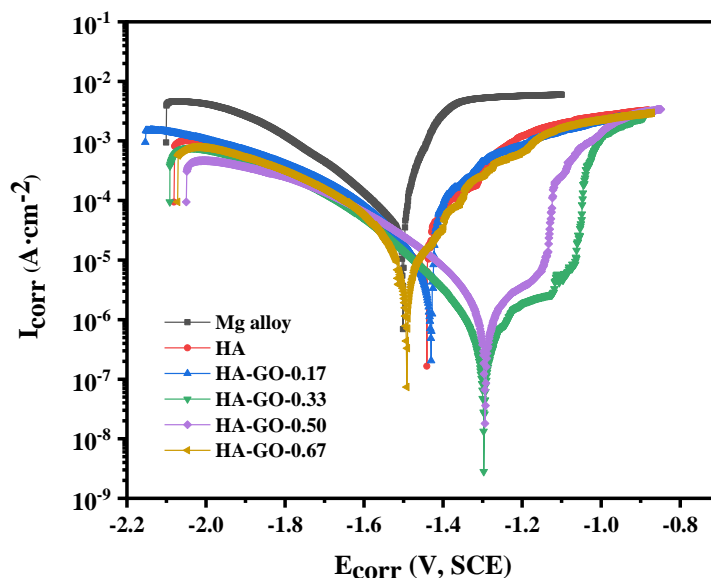

Figure 7. Potentiodynamic polarization curves of different specimens after 48 h immersion in 0.9 wt. % NaCl solution.

Table 2. Electrochemical parameters obtained from Potentiodymanic polarization of different specimens after 48 h immersion in 0.9 wt. % NaCl solution.

Sample	Mg alloy	HA	HA-GO-0.17	HA-GO-0.33	HA-GO-0.50	HA-GO-0.67
E_{corr}(V)	-1.503	-1.441	-1.431	-1.304	-1.293	-1.492
i_{corr}(A.cm^{-2})	5.55×10^{-5}	1.40×10^{-5}	1.31×10^{-5}	5.91×10^{-7}	1.38×10^{-6}	1.16×10^{-5}
IE/%	/	76.1	70.7	99.6	97.4	89.4
E_{bd}(V)	/	-1.318	-1.413	-1.118	-1.134	-1.398
β_a(mV/dec)	35	18	20	13	16	16
β_c(mV/dec)	95	76	95	38	55	66
R_p(Ω.cm^2)	1.81×10^7	4.76×10^7	3.60×10^7	1.47×10^9	3.07×10^8	7.71×10^7

As shown in Fig. 7 and Table 2, the E_{corr} values obtained for AZ91 Mg alloy, HA coating, HA-GO-0.17, HA-GO-0.33, HA-GO-0.50 and HA-GO-0.67 composite coatings were -1.50 V, -1.44 V,   -1.43 V, -1.29 V, -1.30 V and -1.49 V, respectively. AZ91 Mg alloy exhibited a low corrosion potential of -1.50 V. In comparison to AZ91 Mg alloy, the E_{corr} value of composite coatings was slightly increased, implying the limited reduction in corrosion. However, the i_{corr} values of all the

coated AZ91 Mg alloy samples were greater than that of AZ91 Mg alloy. The i_{corr} values for AZ91 Mg alloy, HA coating, HA-GO-0.17, HA-GO-0.33, HA-GO-0.50 and HA-GO-0.67 composite coatings were 5.55×10^{-5}, 1.40×10^{-5}, 1.31×10^{-5}, 5.91×10^{-7}, 1.38×10^{-6} and 1.16×10^{-5} A.cm^{-2}, respectively. It was observed that the i_{corr} values of HA-GO composite coatings, especially HA-GO-0.33, were two orders of magnitude lower than that of HA coating, implying that the chemical stability of the HA coating was further improved by adding the appropriate amount of GO sheets to HA coating. However, the i_{corr} value of HA-GO-0.17 was higher than that of HA coating, because the agglomeration of HA and their non-uniform distribution in the composite coating resulted in a lower barrier protection, as shown in Figs. 6(c) and (d).

Furthermore, the values of R_p, E_{bd} and IE% significantly increased from 1.81×10^{7} Ω.cm^2, -1.318 V and 76.1% for HA coating to 1.47×10^{9} Ω.cm^2, -1.118 V and 99.6% for HA-GO-0.33 composite coating, respectively, which were additional important evidences for the increase of the chemical stability of HA-GO-0.33 composite coating. In addition, from the E_{bd} values in Table 1, it can be found that HA-GO-0.33 composite coating exhibited much higher positive E_{bd} (-1.118 V) than HA-GO-0.50 composite coating (-1.134 V) in the 0.9 wt. % NaCl solution, which signified that the HA-GO-0.33 composite coating demonstrated better local corrosion resistance than HA-GO-0.67 composite coating in the 0.9 wt. % NaCl solution. Based on the above mentioned results, HA-GO-0.33 composite coating was superior in terms of corrosion resistance.

The corrosion behaviors of AZ91 Mg alloy and coated samples in corrosive electrolytes were further investigated using electrochemical impedance spectroscopy (EIS). The EIS Nyquist and Bode plots of AZ91 Mg alloy and coated samples after immersion in the 0.9 wt. % NaCl solution for 48 h are shown in Figs. 8 (a) and (b). The equivalent circuit was applied to fit the plots, as shown in Fig. 9.
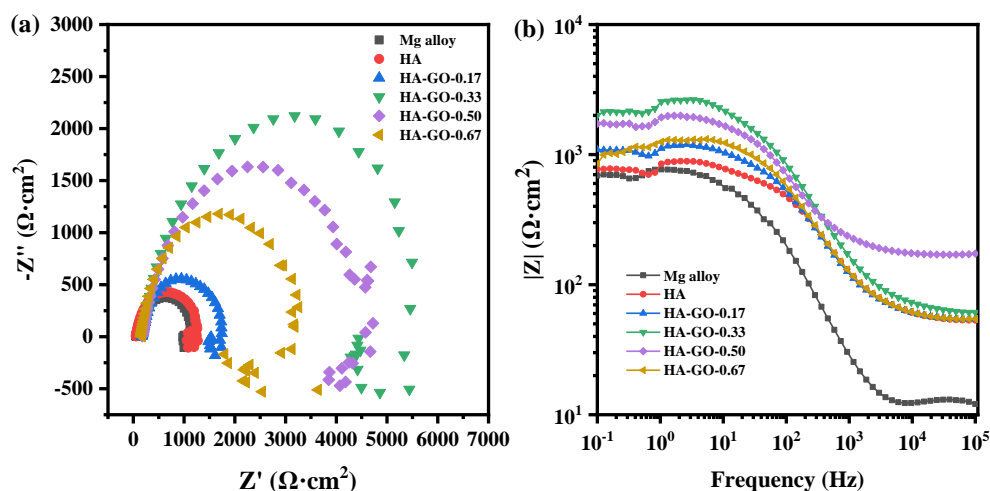

Figure 8. The different specimens after 48 h immersion in 0.9 wt. % NaCl solution. (a) Nyquist plots; (b) Bode plots.
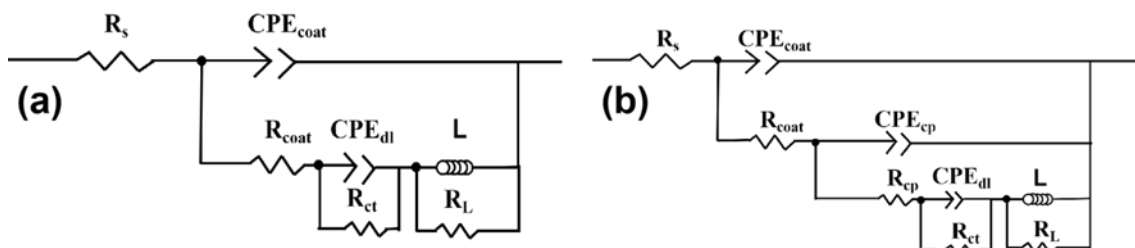
Figure 9. The equivalent circuit obtained by EIS simulation is used to analyze different samples.

Fig. 8(a) shows the Nyquist plots of AZ91 Mg alloy and coated samples in the 0.9 wt. % NaCl solution. The low frequency inductive loop was attributed to occurring pitting corrosion on the surface of AZ91 Mg alloy substrate [81]. In terms of HA coating, HA-GO-0.17 and HA-GO-0.33 composite coatings, the inductive loop was also found in the low frequency range. However, under the same experimental condition, the induction characteristics of HA-GO-0.50 and HA-GO-0.67 composite coatings were not obvious, as shown in Fig. 8(a), indicating that the pitting corrosion of HA-GO-0.50 and HA-GO-0.67 composite coatings was weakened, and further suggesting HA-GO-0.50 and HA-GO-0.67 composite coatings had stronger pitting corrosion resistance than the other coated samples in the 0.9 wt. % NaCl solution.

In general, a high frequency capacitance loop with a larger radius suggests a noticeable enhancement of corrosion resistance of the coated samples [82]. The Nyquist plot of the HA coating was similar to that of AZ91 Mg alloy, indicating a similar corrosion behavior. Comparing with the radius of high frequency capacitance loops in Fig. 8(a), it can be found that with the increase in the content of GO, the radius of the semicircle in Nyquist plot first increased and then decreased, reaching its maximum when the content of GO was maintained at 0.33 mg/mL. However, when the content of GO was further increased, the radius of capacitive loop slightly decreased. The radius of capacitance loops for HA-GO-0.33 composite coating was the largest, indicating the best corrosion resistance among all the samples in the 0.9 wt. % NaCl solution.

Similarly, the same tendency was observed in the Bode impedance plot, as showed in Fig. 8(b). The values of the impedance modulus at a frequency of 0.1 Hz were used to estimate the overall anti-corrosion resistance of the coatings [83,84]. All coatings showed a higher value of $|Z|_{0.1\ Hz}$ than AZ91 Mg alloy (1007 $\Omega.cm^2$). The $|Z|_{0.1\ Hz}$ value of HA coating, HA-GO-0.17, HA-GO-0.33, HA-GO-0.50 and HA-GO-0.67 composite coatings were 1149 $\Omega.cm^2$, 1189 $\Omega.cm^2$, 4192 $\Omega.cm^2$, 1920 $\Omega.cm^2$ and 1155 $\Omega.cm^2$, respectively. According to the results of EIS measurements, the impedance of AZ91 Mg alloy and coated samples decreased in the order: HA-GO-0.33 > HA-GO-0.50 > HA-GO-0.17 > HA-GO-0.67 > HA coating > AZ91 Mg alloy, which is consistent with the polarization test results shown in Fig. 7.

To further understand the electrochemical corrosion behavior of AZ91 Mg alloy and coated samples, the obtained Nyquist plots were analyzed using the equivalent circuit model. Taking into account the micro structural features and chemical heterogeneities of AZ91 Mg alloy and coated samples (shown in Fig. 6), and the typical EIS plots (shown in Fig. 8), EIS equivalent circuits were proposed, as shown in Fig. 9. Two equivalent electrical circuit models shown in Fig. 9(a) corresponded

to uncoated AZ91 Mg alloy and those shown in Fig. 9(b) corresponded to coated samples. The fitting curves and corresponding circuits are presented in Fig. 10, and fitting parameters are listed in Table 3.
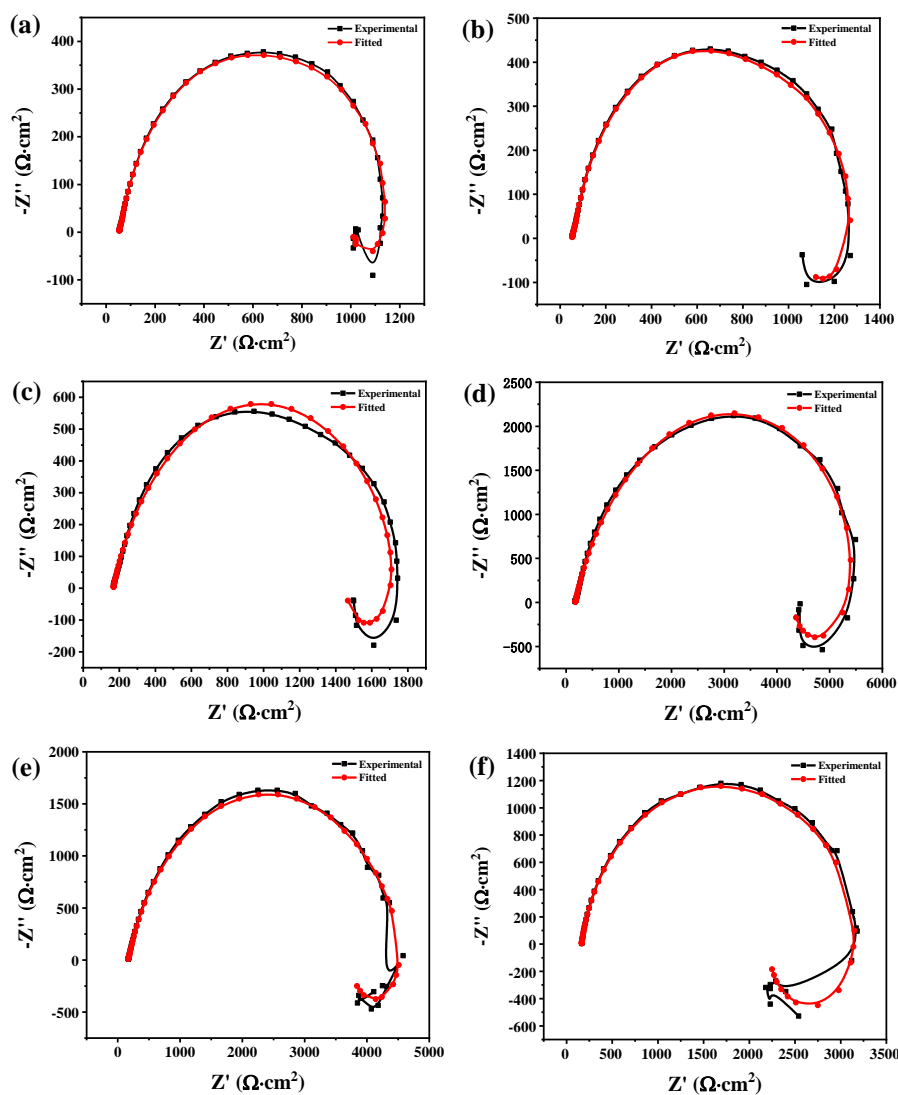

Figure 10. EIS fitting plots of different specimens after 48 h immersion in 0.9 wt. % NaCl solution. (a) AZ91 Mg alloy; (b) HA coating; (c) HA-GO-0.17 composite coating; (d) HA-GO-0.33 composite coating; (e) HA-GO-0.50 composite coating; (f) HA-GO-0.67 composite coating.

In the proposed equivalent circuits, R_s represents solution resistance, R_{coat} represents the layer of corrosive products (uncoated AZ91 Mg alloy) or coating resistance (HA-GO composite coating), and R_{cp} represents the defect resistance such as pores/cracks of coated samples. Herein, because of the non-homogeneity caused by GO interplay in the HA coating, amphiphilic nature of GO sheets, chemical heterogeneities and the formation of carbonated HA in the composite coatings, a pure capacitance was replaced by a constant phase element (CPE) to characterize the non-ideal resistive and capacitance behavior of AZ91 Mg alloy and coated samples [85]. R_{ct} represents the charge transfer resistance, CPE_{dl} represents the non-ideal capacitors of the electrical double layer. The time constant (CPE_{dl}-R_{ct}) is related to the corrosion product layer at the surface of the electrolyte solution/Mg alloy

substrate or the coating/corrosion product layer interface. The inductive behavior characterized by resistance R_L and inductance L suggests the onset of pitting corrosion of AZ91 Mg alloy substrate and coated samples. In this study, CPE was used to replace capacitor (C), due to the consideration of defects in the coating, such as pores/cracks [44].

Table 3. Electrochemical data obtained via equivalent circuit fitting of the EIS curves of different specimens after 48 h immersion in the 0.9 wt. % NaCl solution.

Samples	MG ALLOY	HA	HA-GO-0.17	HA-GO-0.33	HA-GO-0.50	HA-GO-0.67
$R_s(\Omega\cdot cm^2)$	53.0	53.7	165.8	168.1	169.2	163.9
$R_{coat}(\Omega\cdot cm^2)$	648	1255	1730	6163	4591	2876
$C_{coat}(\Omega^{-1}\cdot s^n\cdot cm^{-2})$	9.56×10^{-6}	7.13×10^{-6}	5.74×10^{-6}	6.21×10^{-6}	3.30×10^{-6}	2.39×10^{-6}
$R_{cp}(\Omega\cdot cm^2)$	/	1380	1765	5733	4706	3134
$C_{cp}(\Omega^{-1}\cdot s^n\cdot cm^{-2})$	/	4.60×10^{-7}	4.60×10^{-7}	3.73×10^{-7}	3.60×10^{-7}	3.47×10^{-7}
$R_{ct}(\Omega\cdot cm^2)$	269.1	310.6	341.3	408.6	673.8	947.7
$C_{dl}(\Omega^{-1}\cdot s^n\cdot cm^{-2})$	3.77×10^{-6}	6.30×10^{-5}	6.78×10^{-5}	6.70×10^{-5}	2.01×10^{-6}	1.10×10^{-6}
$R_L(\Omega\cdot cm^2)$	197	300.0	473.0	1205	933.5	1056
L	23.59	40.00	47.52	58.32	156.1	99.2
$R_T (\Omega\cdot cm^2)$	1167.1	3299.3	4475.1	13677.7	11073.5	8177.6
$|Z|(\Omega\cdot cm^2)$	1007	1149	1489	4291	1920	1155

According to the fitting results shown in Table 3, the R_s values of all the coated samples were larger than that of AZ91 Mg alloy in the 0.9 wt. % NaCl solution, suggesting that the reaction between AZ91 Mg alloy and the ions in the NaCl solution was efficiently restrained, which is in good agreement with the Potentiodynamic polarization result (Fig. 7).

As for the coated samples in the 0.9 wt. % NaCl solution, it can be observed from Table 3 that the R_{ct} values of all the coated samples increased with the increase of GO content, which was caused by the decrease in porosity of the loose $Mg(OH)_2$ corrosive products, and consequently a decrease in penetration through corrosive products after the addition of GO to HA coating. Furthermore, with the addition of GO, the values of both R_{coat} and R_{cp} significantly increased until 0.33 mg/mL of the GO content was added. When GO content continued to increase, both values decreased. The increase of R_{cp} revealed that corrosion paths were reduced. However, with the addition of excess GO, the R_{coat} values of HA-GO-0.50 and HA-GO-0.67 coated samples were sharply reduced to 4591 $\Omega.cm^2$ and 2876 $\Omega.cm^2$, respectively, and, the R_{cp} values of the two coated samples were reduced to 4706 $\Omega.cm^2$ and 3134 $\Omega.cm^2$, respectively. According to XRD and FTIR results in Figs. 3 and 5, the value of R_{cp} was higher than that of R_{ct}, it can be suggested that the formation of carbonated HA and precipitated GO-Mg/Ca protective film in pores/cracks of HA-GO composite coatings at the coating and that the layer of corrosive products interface was more corrosion resistant than adsorbed loose corrosive products at the electrolyte solution/Mg alloy substrate surface. The XRD data in Fig. 3 and Table 1 show that the formation of carbonated HA resulted in a slight decrease in the aspect ratio of HA c-axis/a-axis, thus forming a denser structure in HA-GO composite coatings [20]. The denser

composite coatings significantly inhibited the diffusion of aggressive anions in composite coatings to reach Mg alloy substrate, which contributed to lower corrosion rate.

Taking into account the results of Potentiodynamic polarization, EIS, microstructures, the surface porosity, the roles of the formation of carbonated HA and GO-Mg complexes in pores/cracks of HA-GO composite coatings at the composite coatings/corrosive products ($Mg(OH)_2$ film) interface in the NaCl solution . The improvement of the corrosion resistance of HA-GO composite coatings was beneficial to the increase in the micro-pores/crack resistance (R_{cp}) of HA-GO composite coatings or $Mg(OH)_2$ film, as shown in Table 3. The addition of GO to HA coating induced an enhancement of the R_{cp} value, when compared to that of AZ91 Mg alloy and HA coating. R_{cp} was inversely proportional to i_{corr}, as shown in Tables 2 and 3. The values of R_{cp} were one of the most important indexes to evaluate the corrosion protection of HA-GO composite coatings, as precipitated protective film gave a prominent corrosion protection except sizes of the pores/cracks in the composite coatings. The values of R_{cp} were one of the most relevant to evaluate the corrosion protection of the HA-GO composite coatings [85].

The above results suggest that the excellent corrosion resistance was attributed to the increase in the density and compactness of HA-GO composite coatings by filling up the micro-pores and micro-cracks with carbonated HA and GO-Mg composite. Comparing the values of R_{cp} and R_{ct} in the HA-GO composite coatings in the 0.9 wt. % NaCl solution shown in Table 3, it can be observed that, with the increase in the content of GO, the values of R_{cp} first increased and then decreased, reaching its maximum when the content of GO was maintained at 0.33 mg/mL. However, the values of R_{cp} decreased when the content of GO was further increased. In fact, the value of R_{cp} of HA-GO-0.33 composite coating reached the maximum when the content of GO was lower (0.33 mg/mL). The tendency of R_{cp} in the 0.9 wt. % NaCl solution agreed well with that of i_{corr} of HA-GO composite coatings, as shown in Table 2. As shown in Fig. 6, the sizes of micro-pores/cracks in HA coating and HA-GO-0.17 composite coating were larger than that of HA-GO-0.33 composite coating. Some relatively large pores and cracks were covered with GO-Mg composite. However, a great deal of tiny film pores could still be penetrated by water molecule or Cl-. The addition of excess content of GO resulted in an increase in the porosity of HA-GO-0.50 and HA-GO-0.67 composite coatings, but the sizes of micro-pores decreased. In this case, precipitated GO-Mg protective film filling in the micro-pores was much thinner than that in the HA-GO-0.33 composite coating, and the barrier for water molecule or Cl$^-$ was smaller. As a result, water molecule or Cl$^-$ could easily penetrate and corrode AZ91 Mg alloy substrate.

4. CONCLUSIONS

In summary, the electrochemical corrosion results demonstrated that the corrosion protection of HA-GO coated AZ91 Mg alloy in the 0.9 wt. % NaCl solution was significantly dependent on microstructure, surface porosity, the formation of GO-Mg complexes in pores/cracks and precipitation of carbonated HA. The main conclusions are as follows:

(1) The microstructure of HA-GO composite coating with the GO content of 0.17 mg/mL was non-uniform and large particles were observed in some areas. However, with the increase of GO

content, the sizes of HA particles decreased and carbonated HA was formed, making the surface of composite coating more compact and intact.

      (2) In the 0.9 wt. % NaCl solution, the value of E_{corr} (-1.30 V) of HA-GO-0.33 composite coating was significantly higher than that of other coated samples, while the value of i_{corr} (5.91×10^{-7} A.cm^{-2}) was much lower.

References

1. E. L.S. Solomon, A. R. Natarajan, A. M. Roy, V. Sundararaghavan, A. V. der Ven and E. A. Marquis, *Acta Mater.*, 166 (2019) 148-157.
2. J. Singh, M. Kim, J. Lee, H. Guim and S. Choi, *J. Alloys Compd.*, 778 (2019) 124-133.
3. J. Y. Wang, N. Li, R. Alizadeh, M. A. Monclus, Y. W. Cui, J. M. Molina-Aldareguía and J. LLorca, *Acta Mater.*, 170 (2019) 155-165.
4. F. Liu, R. Xin, C. Wang, B. Song and Q. Li, *Scr. Mater.*, 158 (2019) 131-135.
5. B. Manne, H. Thiruvayapati, S. Bontha, R. M. Rangarasaiah, M. Das and V. K. Balla, *Surf. Coat. Technol.*, 347 (2018) 337-349.
6. J. Li, Y. Song, S. Zhang, C. Zhao, F. Zhang, X. Zhang, L. Cao, Q. Fan and T. Tang, *Biomater.*,31 (2010) 5782-5788.
7. N. Hort, Y. Huang, D. Fechner, M. Stormer, C. Blawert, F. Witte, C. Vogt, H. Drücker, R. Willumeit, K. U. Kainer and F. Feyerabend, *Acta Biomater.*, 6 (2010) 1714-1725.
8. R. Shi, J. Miao and A. A. Luo, *Scr. Mater.*, 171 (2019) 92-97.
9. J. Zhao, B. Jiang, Y. Yuan, A. Tang, Q. Wang, T. Yang, G. Huang, D. Zhang and F. Pan, *Mater. Sci. Eng., A.*, 785 (2020) 139344.
10. Y. Wu, Y. Wang, S. Tian, Y. Jing, J. Zhuang, L. Guo, D. Jia and Y. Zhou, *Appl. Surf. Sci.*, 470 (2019) 430-438.
11. H. Kwak and S. Chaudhuri, *J. Alloys Compd.*, 509 (2011) 8189-8198.
12. Z. Zhou, B. Zheng, Y. Gu, C. Shen, J. Wen, Z. Meng, S. Chen, J. Ou and A. Qin, *Surf. Interfaces.*, 19 (2020) 100501.
13. M. Zhang, S. Cai, S. Shen, G. Xu, Y. Li, R. Ling and X. Wu, *J. Alloys Compd.*, 658 (2016) 649-656.
14. S. Mahmoodi, L. Sorkhi, M. Farrokhi-Rad and T. Shahrabi, *Surf. Coat. Technol.*, 216, (2013) 106-114.
15. M. Nakamura, R. Hiratai, T. Hentunen, J. Salonen and K. Yamashita, *ACS Biomater. Sci. Eng.*, 2 (2016) 259-267.
16. E. Boanini, M. Gazzano and A. Bigi, *Acta Biomater.*, 6 (2010) 1882-1894.
17. M. E. Fleet and X. Y. Liu, *J. Solid State Chem.*, 174 (2003) 412-417.
18. M. Aizawa, H. Ueno, K. Itatani and I. Okada, *J. Eur. Ceram. Soc.*, 26 (2006) 501-507.
19. Y. S. Wu, Y. H. Lee and H. C. Chang, *Mater. Sci. Eng. C.*, 29 (2009) 237-241.
20. X. Wei, F. Fu, K. Savino and M. Z. Yates, *Cryst. Growth Des.*, 12 (2012) 3474-3480.
21. J. Cao, Y. Meng, X. Zhao and L. Ye, *Ind. Eng. Chem. Res.*, 59 (2020) 20359-20370.
22. S. Beaufils, T. Rouillon, P. Millet, J. L. Bideau, P. Weiss, J. P. Chopart and A. L. Daltin, *Mater. Sci. Eng. C.*, 98 (2019) 333-346.
23. X. Zhang, G. Song, H. Qiao, J. Lan, B. Wang, H. Yang, L. Ma, S. Wang, Z. Wang, H. Lin, S. Han, S. Kang, X. Chang and Y. Huang, *Colloids Surf., A.*, 603 (2020) 125223.
24. M. Ramadas, G. Bharath, N. Ponpandian and A.M. Ballamurugan, *Mater. Chem. Phys.* , 199 (2017) 179-184.

25. S. R. Garcia, R.Santiago, D. L. Diaz, M. D. Merchan, M. M. Velazquez, J. L. G. Fierro and J. Palomar, *ACS Sustain. Chem. Eng.*, 7 (2019) 12464-12473.
26. Y. Liu, B. Sajjadi, W. Chen and R. Chatterjee, *Fuel.*, 247 (2019) 10-18.
27. R. Saharkhiz, Z. Valefi, M. Mirjani, A. Abdollahi and S. Taghi-Ramezani, *Surf. Coat. Technol.*, 394 (2020) 125818.
28. U. Morali, H. Demiral and S. Sensoz, *Powder Technol.*, 355 (2019) 716-726.
29. D. Chen, J. Colas, F. Mercier, R. Boichot, L. Charpentier, C. Escape, M. Balat-Pichelin and M. Pons, *Surf. Coat. Technol.*, 377 (2019) 124872.
30. V. H. Pham, T. V. Cuong, S. H. Hur, E. W. Shin, J. S. Kim, J. S. Chung and E. J. Kim, *Carbon*, 48 (2010) 1945-1951.
31. A. V. C. Braga, D. C. B. Lago, A. R. Pimenta and L. F. Senna, *Surf. Coat. Technol.*, 372 (2019) 190-200.
32. K. H. Lee, J. Hong, S. J. Kwak, M. Park and J. G. Son, *Carbon*, 83 (2015) 40-47.
33. Y. Chang, W. Zhou, J. Wu, G. Ye, Q. Zhou, D. Li, D. Zhu, T. Li, G. Nie, Y. Du and J. Xu, *Electrochim. Acta.*, 283 (2018) 744-754.
34. K. Krishnamoorthy, K. Jeyasubramanian, M. Premanathan, G. Subbiah, H.S. Shin and S. J. Kim, *Carbon*, 72 (2014) 328-337.
35. N. Karimi, M. Kharaziha and K. Raeissi, *Mater. Sci. Eng. C.*, 98 (2019) 140-152.
36. S. Obregón, G. Amor and A. Vázquez, *Adv. Colloid Interface Sci.*, 269 (2019) 236-255.
37. B.P. Singh, B.K. Jena, S. Bhattacharjee and L. Besra, *Surf. Coat. Technol.,* 232 (2013) 475-481.
38. E. Yılmaz, B. Çakıroğlu, A. Gökçe, F, Findik, H. O. Gulsoy, N. Gulsoy, Ö. Mutlu and M. Özacar, *Mater. Sci. Eng. C.*, 101 (2019) 292-305.
39. P. Bansal, G. Singh and H. S. Sidhu, *Surf. Coat. Technol.,* 401 (2020) 126241.
40. R. Kumari and J. D. Majumdar, *Appl. Surf. Sci.*, 420 (2017) 935-943.
41. G. Gökçeli and N. Karatepe, *Thin Solid Films*, 697 (2020) 137844.
42. W. Du, H. Wu, H. Chen, G. Xu and C. Li, *Carbon*, 158 (2020) 568-579.
43. M. Hwang, M. Kim, S. Kim, Y. C. Kim, H. W. S, J. K. Cho, I. Park, J. Suhr,H. Moon, J. C. Koo, H. R. Choi, K. J. Kim and Y. T. Nam, *Carbon*, 142 (2019) 68-77.
44. S. R. Fardi, H. khorsand, R. Askarnia, R. Pardehkhorram and E. Adabifiroozjaei, *Ceram. Int.*, 46 (2020) 18297-18307.
45. M. Javidi, S. Javadpour, M.E. Bahrololoom and J. Ma, *Mater. Sci. Eng. C.*, 28 (2008) 1509-1515.
46. F. Gao, C. Xu, H. Hu, Q. Wang, Y. Gao, H. Chen, Q. Guo, D. Chen and D. Eder, *Mater. Lett.*, 138 (2015) 25-28.
47. L. Zhang, F. Zhu, H. Li, F. Zhao and S. Li, *Ceram. Int.*, 44 (2018) 21229-21237.
48. M. V. Jaime, J. A. A. Orozco, C. E. D. Ascencio, A. L. S. Robles, M. M. Rosales, A. S. Robles and S. C. Andrade, *J. Environ. Chem. Eng.*, 8 (2020) 104416.
49. A. R. Vatankhah, M. A. Hosseini and S. Malekie, *Appl. Surf. Sci.*, 488 (2019) 671-680.
50. S. M. Prabhu, A. Khan, M. H. Farzana, G. C. Hwang, W. Lee and G. Lee, *J. Mol. Liq.*, 269 (2018) 746-754.
51. S. Yu, J. Liu, W. Zhu, Z. T. Hu, T. T. Lim and X. Yan, *Sci. Rep.*, 5 (2015) 16369.
52. A. Hosseinpour, H. Abdizadeh and M. R. Golobostanfard, *Thin Solid Films*, 631 (2017) 118-123.
53. L. Fathyunes, J. K. Allafi and M. Moosavifar, *J. Mech. Behav. Biomed. Mater.*, 90 (2019) 575-586.
54. Y. Zeng, X. Pei, S. Yang, H. Qin, H. Cai, S. Hu, L. Sui, Q. Wan and J. Wang, *Surf. Coat. Technol.,* 286 (2016) 72-79.
55. X. Zhang, Q. Li, L. Li, P. Zhang, Z. Wang and F. Chen, *Mater. Lett.*, 88 (2012) 76-78.
56. M. Sumathra, K. K. Sadasivuni, S. S. Kumar and M. Rajan, *ACS Omega*, 3 (2018) 14620-14633.
57. R. Sun, M. Li, Y. Lu and A. Wang, *Mater. Charact.*, 56 (2006) 250-254.
58. S. Erakovic, A. Jankovic, D. Veljovic, E. Palcevskis, M. Mitric, T. Stevanovic, D. Janackovic and V. Miskovic-Stankovic, *J. Phys. Chem. B.*, 117 (2013) 1633-1643.

59. R. Balasubramanian and S. Chowdhury, *J. Mater. Chem. A.*, 44 (2015) 21968-21989.
60. E. Iyyappan, S. J. Justin, P. Wilson and A. Palaniappan, *ACS Appl. Nano Mater.*, 3 (2020) 7761-7773.
61. K. Benataya, M. Lakrat, L. L. Elansari and E. Mejdoubi, *Mater. Today: Proc.*, 31 (2020) S83-S88.
62. Y. In, U. Amornkitbamrung, M. Hong and H. Shin, *ACS Omega*, 5 (2020) 27204-27210.
63. W. E. G. Muller, E. Tolba, H. C. Schroder, R. Munoz-Espi, B. Diehl-Seifert and X. Wang, *Acta Biomater.*, 31 (2016) 358-367.
64. T. Tsoufis, F. Katsaros, Z. Sideratou, G. Romanos, O. Ivashenko, P. Rudolf, B. J. Kooi, S. Papageorgiou and M. A. Karakassides, *Chem. Commun.*, 50 (2014) 10967-10970.
65. S. Lee and S. Park, *Carbon*, 68 (2014) 112-117.
66. H. Khallok, A. Elouahli, S. Ojala, R. L. Keiski, A. Kheribech and Z. Hatim, *Ceram. Int.*, 46 (2020) 22581-22591.
67. H. Nishikawa, T. Oka, N. Asai, H. Simomichi, T. Shirai and M. Fuji, *Appl. Surf. Sci.*, 258 (2012) 5370-5374.
68. M. Mahdavi, M. Ahmad, M. Haron, F.Namvar, B. Nadi, M. Rahman and J. Amin, *Molecules*, 18 (2013) 7533-7548.
69. N. Kamiyama, G. Panomsuwan, E. Yamamoto, T. Sudare, N. Saito and T. Ishizaki, *Surf. Coat. Technol.,* 286 (2016) 172-177.
70. C. Ning, L. Zhou, Y. Zhu, Y. Li, P. Yu, S. Wang, T. He, W. Li, G. Tan, Y. Wang and C. Mao, *Langmuir*, 31 (2015) 13561-13570.
71. Z. Mao, X. Yang, S. Zhu, Z. Cui and Z. Li, *Ceram. Int.*, 41 (2015) 3461-3468.
72. W. L. Suchanek, K. Byrappa, P. Shuk, R.E. Riman, V.F. Janas and K.S. Tenhuisen, *Biomater*, 25 (2004) 4647-4657.
73. H. Khallok, A. Elouhli, S. Ojala, R. L. Keiski, A. Kheribech and Z. Hatim, *Ceram. Int.*, 46 (2020) 22581-22591.
74. M. Xie, M.O. Olderoy, J. Andreassen, S. M. Selbach, B. L. Strand and P. Sikorski, *Acta Biomater.*, 6 (2010) 3665-3675.
75. T. Moskalewicz, M. Warcaba, L. Cieniek, M. Sitarz, M. Gajewska and A. R. Boccaccini, *Appl. Surf. Sci.*, 540 (2021) 148353.
76. D. Ramani and T. P. Sastry, *Cellulose*, 21 (2014) 3585-3595.
77. C. Wen, X. Zhan, X. Huang, F. Xu, L. Luo and C. Xia, *Surf. Coat. Technol.*, 317 (2017) 125-133.
78. J. Liang, P. B. Srinivasan, C. Blawert and W. Dietzel, *Electrochim. Acta.*, 55 (2010) 6802-6811.
79. S. M. Emaratia and M. Mozammel, *Ceram. Int.*, 46 (2020) 1652-1661.
80. G. Achary, Y. A. Naik, S. V. Kumar, T. V. Venkatesha and B. S. Sherigara, *Appl. Surf. Sci.*, 254 (2008) 5569-5573.
81. JA Li, L Chen, XQ Zhang and SK Guan, *Mater. Sci. Eng., C*, 2019, 109:110607.
82. J Song, C Shu, F Zhang, X Peng, L Rui, L Yue, Y Jiang and G Xu, *Mater. Sci. Eng., C*, 2018, 91(OCT):218-227.
83. K. Abdi-Alghanab, D. Seifzadeh, Z. Rajabalizadeh and AH. Yangjeh, *Surf. Coat. Technol.*, 2020:125979.
84. C. JHCAB, B. LBTA, C. MW, C. ZHJ, A. DNZ, A. SFL and B. HJZ, *Carbon*, 2020, 161:577-589.
85. B. K. Jiang, A.Y. Chen, J. F. Gu, J. T. Tan, Y. Liu, P. Wang, H. J. Li, H. Sun, J. H. Yang and X. Y. Wang, *Carbon*, 157 (2020) 537-548.